



BHPA-symposium 2022

Scientific Committee

Milan Tomsej (chair), CHU Charleroi

Alain Seret, Université de Liège

Caro Franck, Universitair Ziekenhuis Antwerpen

Damien Dumont, UCLouvain

Kristof Baete, KU Leuven

Lara Struelens, SCK-CEN

Federica Zanca, Palindromo

Koen Tournel, Jessa Ziekenhuis

Nico Buls, UZ Brussel

Gert Van Gompel, UZ Brussel

Thierry Gevaert, UZ Brussel

Scientific Session

Topic: X-ray Imaging

Chair: Hilde Bosmans (KU Leuven)

Friday 29/04/2022 11h00-12h15

Room 11 - 22

Multicenter study on scanning outside the localizer borders in chest CT

A. Dedulle^{1,2}, N. Fitousi¹, Y. De Bruecker³, M. Cannie⁴, A. Houben⁵, T. Roland⁶, C. Vanreppelen⁷, M. Willocxand⁸, J.Binst⁹, H. Bosmans^{2,9},

¹ *Qaelum NV, Belgium*

² *University Leuven, Belgium*

³ *Imelda vzw, Belgium*

⁴ *CHU Brugmann, Belgium*

⁵ *Ziekenhuis Oost-Limburg, Belgium*

⁶ *AZ Diest, Belgium*

⁷ *Regional hospital Sint-Trudo, Belgium*

⁸ *OLV Ziekenhuis, Belgium*

⁹ *University Hospitals Leuven, Belgium*

ABSTRACT

KEY WORDS – Chest CT, scan length, blind scan

Introduction

Blind scan in CT imaging is when the scan range goes outside the localizer borders. Without the localizer information, the tube current modulation (TCM) cannot be optimally applied as there is limited information about the attenuation properties of the blind area. This could have an influence on the dose, especially to sensitive structures, like the thyroid, when they are part of the blind scanning. Advanced dose management systems focus on all quality aspects of an imaging exam, including the assessment of blind scan. The purpose of this study was to evaluate the blind scanning of chest CT examinations in a number of Belgian imaging centers. Additionally, the influence of tube current modulation on the thyroid dose was investigated in order to estimate the excess radiation burden that blind scan could cause.

Materials and methods

Retrospective chest CT data from eight hospitals (16 scanners) and a period of two years were collected. The same dose management software (DOSE, Qaelum, Belgium) is used in all participating centers, so the calculated parameters follow the same methodology. Extracted data included the top and lower blind scan (towards neck and abdomen respectively), as well as the scan length. The data comparison was performed with a Kruskal-Wallis test (significance level of 0.05).

Next, a theoretical study was performed to evaluate the thyroid dose in different clinical settings to highlight the impact of potential blind scan on the thyroid dose. Simulations with a dosimetric tool integrated in the dose

management software were performed. All simulations were performed twice; with and without tube current modulation (TCM):

1. Standard chest CT with the thyroid outside of the scan range.
2. Extended scan range with 1/3 of the thyroid included.
3. Extended scan range with the complete thyroid included.

Results

The complete dataset included 55476 CT acquisitions. The scan lengths used in the centers were significantly different ($p < 0.05$), with median scan lengths ranging from 35cm to 42cm. The frequency of blind scan towards the abdomen was low, it occurred in less than 1.5% for each center. On the other hand, the frequency of blind scan towards the neck region was substantial, ranging from 5% to 21% for the different centers. The amount of blind scan was significantly different ($p < 0.05$) between the centers, with median values ranging from 16mm to 20mm. The frequency of acquisitions with blind scan above 30mm ranged from 1% to 6% (Table 1).

In the theoretical study, the simulations with TCM showed that the thyroid dose increased with 13% if partially irradiated and with 107% when fully irradiated compared to a scan range without the thyroid included. Without TCM, the thyroid dose increased with 49% when partially included and with more than 600% when fully irradiated.

Table 1: Summary of the median scan length (SL) and blind scan (BS) for each participating site. Also, the occurrence frequency of the lower blind scan, top blind scan and the top blind scan above 30mm for each site are included.

Site	median SL (cm)	median BS (mm)	BS lower	BS top	BS top >30mm
A	38	17	1.3%	14%	3%
B	42	18	0.6%	12%	3%
C	36	21	0.5%	21%	6%
D	40	17	0.3%	9%	1%
E	37	17	0.2%	5%	1%
F	35	18	0.5%	17%	4%
G	40	16	0.2%	5%	1%
H	37	16	0.7%	10%	2%

Conclusion

The frequency and amount of blind scan is significantly different between centers. Including the thyroid in the scan range can double the thyroid dose. Additionally, the tube current modulation might be compromised in the blind scan area, leading to a fourfold of the thyroid dose. Extra training of the operators with clear examples of the impact of blind scan will help to optimize the scanning technique and create dose awareness.

Image quality evaluation of an intraoperative portable CT system in cochlear implantation surgery

E. Verelst¹, Dr. V. Topsakal¹, B. Keelson¹, G. Van Gompel¹, N. Buls¹

¹Vrije Universiteit Brussel (VUB), Universitair Ziekenhuis Brussel (UZ Brussel), Radiology department, Laarbeeklaan 101, 1090 Brussel, Belgium

ABSTRACT – Intraoperative scanning of the inner ear is routinely performed with cone-beam CT (CBCT) systems. These systems are desired to have high accuracy and image quality as they play a key role in image guided robotic procedures. To evaluate the image quality of such systems, a comparison is made with other CT and CBCT systems using a reference CATPHAN CT-QC phantom in parallel with CTDI measurements. Clear differences in image quality were observed between both the systems and different low/high dose protocols.

KEY WORDS – Intraoperative imaging, portable CBCT scanner, image guided robotic procedures, inner ear surgery, image quality

Introduction

Inner ear surgical procedures require precise and safe management¹. Advances in imaging techniques combined with robotic technology offer the opportunity to transform inner ear surgeries to keyhole procedures². Intraoperative scanning is capable of guiding robotic technology. Recognizing the functionally important inner ear structures requires high accuracy in terms of image quality³. For this high precision otological imaging, CBCT is preferable as it is characterized with high spatial resolution and low radiation dose⁴.

Materials and methods

The Xoran xCAT IQ system (*Xoran Technologies inc.*, US) was compared with three other clinical (CB)CT systems: NewTom5G CBCT (*NewTom*, Italy), Philips Azurion Clarity IQ (*Philips HealthCare*, The Netherlands) and GE Revolution CT (*GE HealthCare*, US). Image quality was analyzed using a dedicated phantom. The CATPHAN 504 phantom (*The Phantom Laboratory*, UK) was scanned on all four devices using two clinical used protocols for head imaging. Parallel with image acquisition, CTDI measurements were performed using a 100 mm pencil beam ionization chamber (*RTI Group*, Sweden) placed in a 16 cm CTDI head phantom. The CTDI measurements served as a guidance for the comparison. Imaging protocols resulting in CTDI_{100,c} values close to values from the two protocols on the Xoran xCAT were used for comparison. Image quality analysis was performed using ImageJ. The uniformity index (UI) was used for the evaluation of uniformity and was calculated as

$$UI = \left| \frac{S(ROI_p) - S(ROI_c)}{S(ROI_c)} \right|,$$

where S(ROI) is the mean CT number in respectively peripheral (p) and central (c) regions of interest (ROI). For the UI, absolute values are considered.

Image homogeneity or noise was quantified by using the standard deviation (SD) of the mean CT number in a central ROI. To make a comparison possible between the different systems, the noise value was standardized and expressed as a percentage. High spatial resolution was evaluated using the CATPHAN504 CTP528 module line pair (lp) inserts. The CATPHAN 504 CTP404 module was used to assess the linearity of the system. Observational evaluation of streak and ring artefacts was eventually performed.

Results

An overview of the results can be found in table 1. A high and low dose protocol was selected for each system based on CTDI_{100,c} measurements. Results of the UI demonstrated a higher

uniformity for the CT system (GE Revolution) with an UI of 0,19, compared to the Philips Azurion CBCT protocols and the NewTom5G CBCT system, where respectively UI values of 0,34, 0,24 and 3,76, 2,42 were calculated. Graphical representation confirms these results. As lower CT numbers in the central ROI were observed, lower uniformity scores can be traced back to beam hardening effects. Noise results, depicted in table 1, show a decreasing noise value for higher mAs values and CTDI_{100,c} values except for the Philips Azurion CBCT protocols. A higher percentage of noise was observed for higher mAs values. Considering CT linearity, the Philips Azurion was found to have the highest extent of linearity ($R^2 = 0,999$). For the NewTom5G CBCT system, results were inconsistent as the lower dose protocol resulted in an R^2 value of 0,732 and the higher dose protocol in an R^2 value of 0,998. The NewTom5G CBCT system was found to have the highest spatial resolution. Lower high spatial resolution was observed for the Philips Azurion system and the GE Revolution CT. Lastly, beam hardening streak artefacts were found in the CATPHAN modules where high density materials were present. This was the most pronounced in the NewTom5G images. The GE Revolution CT system showed less beam hardening streak artefacts. The presence of ring artefacts follow these observations as they were more pronounced in the NewTom5G CBCT images compared to the other two systems.

Table 1: Overview image quality analysis results with corresponding protocol exposure settings. CTDI_{100,c} measurements for the GE Revolution CT are missing due to incompatible measurement equipment and protocol/exposure settings.

System	protocol	kV	mAs	CTDI _{100,c} (mGycm)	UI	Noise (%)	high spatial resolution (lp)	linearity (R ²)	artefacts
NewTom5G	ecoscan	110	12,22	23,38	3,76	3,85	15	0,732	Streak & ring artefacts
	enhanced boost	110	61,43	91,34	2,42	1,32	16	0,998	Streak & ring artefacts
Philips Azurion	CBCT HQ 60fps (10s)	120	15,82	307,49	0,39	1,08	8	0,999	Limited streak & ring artefacts
	CBCT LD 60fps (5s)	120	32,04	153,49	0,24	1,37	7	0,999	Limited streak & ring artefacts
GE Revolution CT	Head RT 1mm	120	4,84		0,19	0,72	7	0,998	Limited ring artefacts
	Head RT 3mm	120	7,48		0,19	0,57	7	0,998	Limited ring artefacts

Conclusion

In terms of high spatial resolution, CBCT tends to be superior compared to a CT system. However, the higher spatial resolution comes at a cost of longer scan times less uniformity and more pronounced artefacts. In the field of intraoperative scanning, the high spatial resolution is preferable as the images are used for the guidance of the robotic system.

References

1. Conley, D. B. *et al.* Comparison of intraoperative portable CT scanners in skull base and endoscopic sinus surgery: Single center case series. *Skull Base* **21**, 261–270 (2011).
2. Caversaccio, M. *et al.* Robotic middle ear access for cochlear implantation: First in man. *PLoS ONE* **14**, (2019).
3. Rafferty, M. A. *et al.* Intraoperative cone-beam CT for guidance of temporal bone surgery. *Otolaryngology - Head and Neck Surgery* **134**, 801–808 (2006).
4. Nardi, C. *et al.* Head and neck effective dose and quantitative assessment of image quality: A study to compare cone beam CT and multislice spiral CT. *Dentomaxillofacial Radiology* **46**, (2017).

Determination of X-ray spectra and modelling of shaped filters – Influence on simulated CT organ dose

Gwenny Verfaillie¹, Yves D'Asseler^{1,2}, Klaus Bacher¹

¹Ghent University, Belgium; ²Ghent University Hospital, Belgium

ABSTRACT – For patient-specific CT organ doses determinations, the best results are obtained when manufacturer's data on the X-ray spectrum and bowtie filter are used in a Monte Carlo simulation. Current study shows that dose differences within 6% are found when other spectrum and bowtie filter determination methods are used.

KEY WORDS – Nuclear medicine, CT, Monte Carlo, Organ dose

Introduction

Monte Carlo frameworks are the gold standard to perform patient-specific CT dosimetry because they allow an accurate description of the CT scanner and the implementation of anatomical models. To obtain the best results, quantitative spectral information and information on the bowtie filter material and shape is provided by the manufacturer. However, manufacturer's data are not always available. In this study, the influence of different X-ray spectrum determination and shaped filter modelling methods on simulated CT organ doses is studied.

Materials and methods

As part of the Horizon 2020 MEDIRAD project, the Monte Carlo software ImpactMC was used. X-ray spectra were created based on quantitative information from the manufacturer, the integrated ImpactMC and SpekCalc spectrum generator, and half-value layer measurements combined with the SPEKTR tool applying a voltage ripple of 0% and 25% (Figure 1). The bowtie filter models are based on manufacturer's data and measured dose values. For each out of ten X-ray spectrum and bowtie filter combinations, the impact on simulated CT organ doses was studied for twenty adult patients (10 female and 10 male patients) undergoing a diagnostic CT scan at 120 kV with tube current modulation as part of a whole-body PET/CT examination.

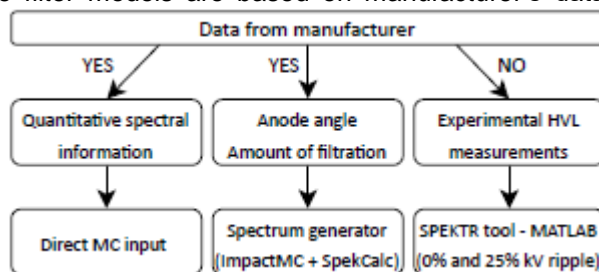


Figure 1: Overview of the obtained X-ray spectra.

Results

The estimated CT organ doses are the smallest and largest when using the X-ray spectrum provided by the manufacturer and generated with SpekCalc, respectively. However, for all spectra and irrespective from the used bowtie model, organ doses are within 6% from those resulting from simulations with the manufacturer's spectrum. Applying the bowtie model of the manufacturer results in lower doses for most organs. Overall, differences in CT organ doses are smaller than 1% when modelling the bowtie filter based on dose measurements while keeping the X-ray spectrum constant. For all X-ray spectrum and bowtie filter combinations, organ doses are within 6% from those resulting from simulations with the spectrum and bowtie model provided by the manufacturer (Figure 2). Disregarding all situations using quantitative manufacturer's data, the best results are obtained by determining equivalent energy spectra with a voltage ripple of 0% and model the bowtie filter based on dose measurements. Organ dose differences are then within 3%.

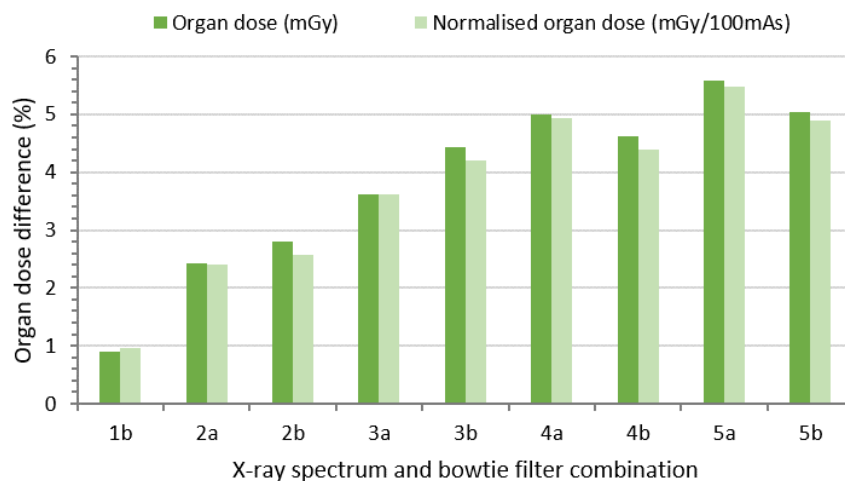


Figure 2: Maximum organ dose difference for all X-ray spectrum and bowtie filter combinations compared to combination 1a ('1' = manufacturer's spectrum, '2' = equivalent spectrum with 0% voltage ripple, '3' = equivalent spectrum with 25% voltage ripple, '4' = spectrum ImpactMC generator, '5' = SpekCalc spectrum, 'a' = bowtie model manufacturer, 'b' = bowtie model based on dose measurements).

Conclusion

When manufacturer's data is not available, half-value layer and dose measurements provide sufficient input to obtain equivalent X-ray spectra and bowtie filter profiles, respectively. Monte Carlo simulations then result in estimated CT organ doses that deviate less than 6% from the most accurate simulations.

Acknowledgements - This project has received funding from the Euratom research and training programme 2014-2018 under grant agreement No 755523.

Combined Assessment of Blood Flow and Tissue Perfusion in Diabetic Feet Using Intra-arterial 4D Contrast CT Angiography and Perfusion

P. T. Boonen^{1,2,3}, N. Buls¹, J. Vandemeulebroucke^{2,3}, G. van Gompel¹, F. Van den Bergh¹, D. Aerden⁴, J. De Mey¹

¹Department of Radiology, Vrije Universiteit Brussel (VUB), Laarbeeklaan 101, 1090 Brussels, Belgium

²Department of Electronics and Informatics (ETRO), Vrije Universiteit Brussel (VUB), Pleinlaan 2, 1050 Brussels, Belgium

³imec, Kapeldreef 75, 3001 Leuven, Belgium

⁴Department of Vascular Surgery, Vrije Universiteit Brussel (VUB), Laarbeeklaan 101, 1090 Brussels, Belgium

ABSTRACT

The aim of this study is to employ dynamic computed tomography angiography (CTA) imaging and perfusion (CTP) imaging for improved anatomic and hemodynamic information in patients with foot ulcers for optimal treatment planning using low-volume intra-arterial contrast injections. To this end, three patients with clinically suspected peripheral arterial disease (PAD) showing small necrotic foot ulcers received a 4D CT examination combined with an IADSA examination. Arterial blood flow and flow perfusion values were assessed from the CT data and were compared for healthy tissue and wounds.

KEY WORDS – Peripheral Arterial Disease, Computed Tomography, Perfusion, Hemodynamics, Diabetes

Introduction

Peripheral arterial disease (PAD) is a chronic atherosclerotic process which causes a partial or complete obstruction in the peripheral arteries legs [1, 2]. Patients with diabetes have a two- to fourfold increased risk of developing PAD compared to non-diabetic individuals [3]. It is estimated that over time, 20% of patients suffering from PAD will develop critical limb ischemia (CLI), characterized by high mortality and irreversible damage to the leg which results in a high incidence of lower extremity amputations in people with diabetes [4]. Intra-arterial digital subtraction angiography (IADSA) has been the gold standard for the examination of

the below-the-knee arterial tree but recent improvements for wide beam CT allow successive CT acquisitions over 160 mm at high temporal resolution. We propose a new methodology for diagnosing CLI by employing computed tomography angiography (CTA) imaging and computed tomography perfusion (CTP).

Materials and methods

Dynamic 4D CT data (Aquilion ONE Genesis, Canon) of the ankle and feet were acquired during IADSA examinations of the lower extremities. During these examinations, a Simmons-2, 5 Fr Catheter (Cook Medical) was introduced into the external iliac. At the start of the CT acquisitions, two mL of contrast agent (Ultravist 370) diluted with 18 mL of saline was injected at a rate of 4.0 mL/s during 5 s.

The combined CTA and CTP protocol consisted of multiple 160 mm axial series at 0.52 s tube rotation. Firstly, a 40 s continuous acquisition was performed, followed by 16 repeated acquisitions with a 2 s interphase delay and 7 acquisitions using a 5 s interval. Finally, 6 additional acquisitions were made at a 15 s interval to capture the tissue perfusion. The total scan time was 194 s.

The foot was segmented into five volumes of interest (VOI), according to the angiosome concept [5]. Their corresponding input arteries were determined, and time-attenuation curves were automatically generated to calculate the arrival time of the contrast bolus (TTP). A voxel-wise assessment of the blood flow was performed using the slope method and the arterial input function. Perfusion values (mL/g.s) of healthy tissue and wounds were compared using a Mann-Whitney U test (SPSS, IBM).

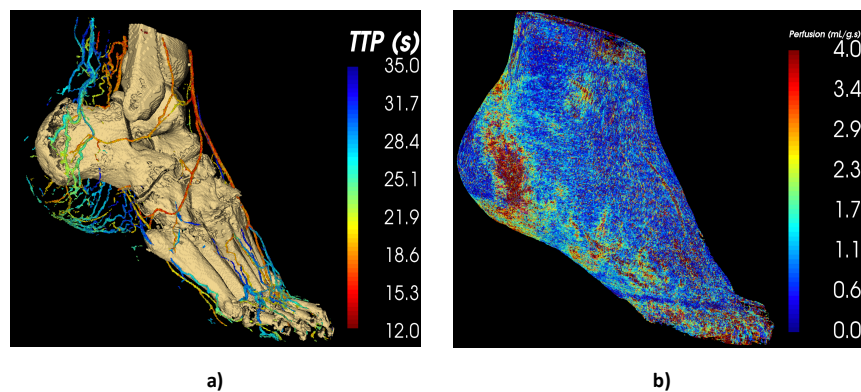


Figure 1: Left: parametric map indicating the contrast arrival time (TTP) for blood vessels by means of a color-code. Right: parametric blood flow map indicating perfusion values (mL/g.s) by means of a color-code.

Results

Three patients with clinically suspected PAD showing small necrotic foot ulcers received a 4D CT combined with an IADSA examination. Blood flow was assessed successfully and based on the TTP values, arteries and veins could clearly be distinguished (Figure 1a). In all patients, the perfusion values (mL/g.s) in the affected tissue were significantly higher ($p < 0.001$) compared to adjacent healthy areas (Table 1 & Figure 1b).

Table 1: Median blood flow perfusion values for wounds and adjacent healthy tissue derived from 4D CT imaging using the slope method.

Case	Healthy tissue		Wounds		P
	Perfusion (mL/ g.s)	95% CI	Perfusion (mL/ g.s)	95% CI	
1	0.87	[0.83 - 0.92]	1.44	[1.32 - 1.54]	<0.001
2	0.96	[0.88 - 1.04]	4.81	[4.79 - 5.05]	<0.001
3	1.28	[1.20 - 1.36]	3.89	[3.68 - 4.10]	<0.001

Conclusion

The 4D CT protocol combined with the minimal usage of contrast agent (2 mL) provides novel information as three phases (arterial, perfusion and venous) are captured in 3D. The obtained hemodynamic parameters allow for an improved diagnosis of critical limb ischemia which can be used to optimize treatment planning.

References

- [1] Boyko EJ, Monteiro-Soares M, Wheeler SGB. Peripheral Arterial Disease, Foot Ulcers, Lower Extremity Amputations, and Diabetes. In: Cowie CC, Casagrande SS, Menke A, al., editors. Diabetes in America. 3rd edition. Bethesda (MD): National Institute of Diabetes and Digestive and Kidney Diseases (US); 2018 Aug. CHAPTER 20.
- [2] Mascarenhas JV, Albayati MA, Shearman CP, Jude EB. Peripheral arterial disease. *Endocrinol Metab Clin North Am.* 2014 Mar;43(1):149-66. doi: 10.1016/j.ecl.2013.09.003. PMID: 24582096
- [3] M.Á. Tresierra-Ayala, A. García Rojas, Association between peripheral arterial disease and diabetic foot ulcers in patients with diabetes mellitus type 2, *Medicina Universitaria*, Volume 19, Issue 76 2017, Pages 123-126, ISSN 1665-5796, <https://doi.org/10.1016/j.rmu.2017.07.002>
- [4] Criqui MH, Matsushita K, Aboyans V, Hess CN, Hicks CW, Kwan TW, McDermott MM, Misra S, Ujueta F; Lower extremity peripheral artery disease: contemporary epidemiology, management gaps, and future directions: a scientific statement from the American Heart Association. *Circulation.* 2021;144:e171–e191. doi: 10.1161/CIR.0000000000001005
- [5] Attinger CE, Evans KK, Bulan E, Blume P, Cooper P. Angiosomes of the foot and ankle and clinical implications for limb salvage: reconstruction, incisions, and revascularization. *Plast Reconstr Surg.* 2006 Jun;117(7 Suppl):261S-293S. doi: 10.1097/01.prs.0000222582.84385.54. PMID: 16799395.

Evaluation of Virtual Grid processed clinical chest radiographs

T. Gossye¹, D. Buytaert², K. Bacher¹

¹*Ghent University, Belgium*

²*Cardiovascular Center Aalst, Belgium*

ABSTRACT – Virtual Grid software is developed to improve the image quality of gridless radiographs. We evaluated the radiographs obtained with various Virtual Grid settings of 50 patients by human observers and software algorithms. As seen by the human observers and the software algorithms, Virtual Grid improves the IQ of chest bedside radiographs.

KEY WORDS – Software-based scatter correction; Chest radiography; Mobile radiography unit; Image quality,

Introduction

Bedside chest x-ray examinations are performed daily in the intensive care unit (ICU) for follow-up of patients with respiratory and/or cardiovascular illness. It is uncommon to use physical grids for bedside examinations due to the difficult circumstances where technologists operate and the high likelihood of positioning errors.¹ To improve the image quality (IQ) of the radiographs obtained without a physical grid (gridless), Fujifilm (Tokyo, Japan) developed software (SW), commercially known as Virtual Grid.² We evaluated the different Virtual Grid software grid ratios (Fujifilm, Tokyo, Japan) on gridless clinical chest radiographs with visual grading analysis (VGA). In addition, we investigated the 2 image quality assessment algorithms (IQAAs).

Materials and methods

Chest radiographs of 50 different intensive care unit (ICU) patients were collected and afterwards processed with Virtual Grid software. Different software grid ratios—6:1, 10:1, 13:1, 17:1, and 20:1—were applied to investigate the image quality (IQ) improvement. IQ improvement was assessed by 4 radiologists in a relative VGA study. One of the IQAA used to analyze the radiographs was implemented in our department but was originally developed by the research group of the Duke University Medical Center³. A general IQ score (IQS) was calculated based on the metrics contrast, detail, and noise. Another IQAA—naturalness image quality evaluator (NIQE)—available in Matlab (MATLAB Research R2019b, the MathWorks, Inc.) was evaluated. Both methods were compared with VGA.

Results

VGA scores of gridless radiographs are significantly lower ($P < 0.001$). IQ increases with increasing software grid ratios, up to grid ratio 17:1 (Table 1). However, some anatomical structures—spine and ribs—are negatively affected by the higher grid ratios. A correlation coefficient of 0.99 between the VGA and the IQS was observed. The correlation coefficient between VGA and NIQE was 1.00.

Table 1: influence of Virtual Grid grid ratios on IQ

Virtual Grid SW grid ratios						
	0	6:1	10:1	13:1	17:1	20:1
VGA	-0.96	-0.14	0.01	0.08	0.09	0.09
IQS	-0.39	-0.05	0.00	0.03	0.06	0.08
NIQE	-0.32	-0.02	0.00	0.02	0.03	0.04

Conclusion

Virtual Grid improves the IQ of chest bedside radiographs. The higher grid ratios should be considered carefully as the software increases the noise, which negatively affects the visibility of the bone structures. Therefore, grid ratios up to 13:1 can be advised. The IQAAs are promising and could be used to detect differences in IQ when different Virtual Grid software settings are used.

References

- [1] Gauntt DM, Barnes GT. An automatic and accurate x-ray tube focal spot/grid alignment system for mobile radiography: system description and alignment accuracy. *Med Phys.* 2010;37(12):6402-10.
- [2] Kawamura T, Naito S, Okano K, et al. Improvement in Image Quality and Workflow of X-Ray Examination using a New Image Processing Method, "Virtual Grid Technology". Imaging Technology Center; 2014.
- [3] Lin Y, Luo H, Dobbins JT, et al. An image-based technique to assess the perceptual quality of clinical chest radiographs. *Medical physics.* 2012;39(11):7019-31

Dynamic CT imaging in revalidation tracking of jaw movements: A feasibility study.

B. Keelson¹, S. Huys^{2,3}, Y. de Brucker¹, G. Van Gompel¹, J. de Mey¹, J. Vander Sloten², M Mommaerts¹, S. Héréus⁴, N. Buls¹

¹*Universitair Ziekenhuis Brussel (UZ Brussel), Vrije Universiteit Brussel (VUB), Belgium*

²*Catholic University of Leuven, Belgium*

³*CADskills BV, Belgium*

⁴*Vrije Universiteit Brussel (VUB), Belgium, Country*

ABSTRACT

The possibilities of using 4D CT-scanning for the tracking of patients' revalidation progress after a total temporomandibular joint replacement (TMJR) was assessed. A phantom was used to simulate mandibular motion and scanned five times with a dynamic CT acquisition protocol. An image processing workflow was developed to extract kinematic parameters from the dynamic sequences. Promising steps were taking in developing a framework to use 4D CT-scanning as a usable methodology to improve the follow-up during the revalidation of patients that underwent a total temporomandibular joint replacement.

KEY WORDS – Dynamic CT, TMJR, Image registration

Introduction

The temporomandibular joints (TMJ's) are very complex and unique joints in the human body. This joint consists of a hinge and slide (rotation and translation) motion during its operation. While most disorders of this joint can be treated with minimally or non-invasive surgeries, some patients may require total temporomandibular joint prosthesis. Patients that undergo such procedures usually have limited movement capabilities due to inflammation, swelling, pain and stiffness. Post-operative physiotherapy plays an important role in achieving good postoperative results [1], hence the monitoring of the revalidation process of such patients is vital. Current approaches to evaluate mandibular movement lack a detailed analysis of the condylar behaviour during movement. This renders them inadequate for evaluating revalidation progress of the patient. This gap can be filled using dynamic 4D CT-scanning, which adds a time dimension to 3D images. The goal of this experimental phantom study was therefore to evaluate the feasibility of using dynamic CT-scans to track the progress of rehabilitating TMJ patients by recording the motion of this joint.

Materials and methods

A 3D printed phantom was developed to simulate mandibular movements repetitively and with variable speeds. A clinical 256-slice Revolution CT (GE Healthcare, Waukesha, Wisconsin, USA) was used in obtaining continuous volume scans without table movement while the phantom was in motion. Tube rotation time was 0.28 s, tube voltage was 80 kVp, tube current 50 mA and 16 cm collimation in the z-axis direction. This resulted in a scan duration of 6 seconds. Images were reconstructed with a slice thickness of 1.25 mm, a 200 mm field of view and a 512 x 512 x 128 image matrix. The phantom was scanned five times for repeatability. Kinematic parameters (Cardan angles and displacements) were obtained by a pairwise rigid registration of the image data from each time point in the dynamic scan sequence with a manually selected reference image within the sequence. The 95% confidence interval of the estimated kinematic parameters across all time points for the five repetitions was evaluated as a measure of reproducibility. The Dose Length Product (DLP) and $CTDI_{vol}$ were recorded and potential patient effective dose was calculated based on a detailed voxel based dosimetry model by the National Cancer Institute [3]

Results

The average 95% confidence interval for the displacement across all time points for the five repetitions was 0.41 mm, 0.61 mm and 0.20 mm for the X, Y and Z axis respectively. In terms of rotations, average 95% confidence interval across all time points for the five repetitions were 1.39°, 0.31° and 1.29° for the X, Y and Z axis respectively. The estimated effective dose for the dynamic scan was found to be 1.3 mSv, for a $CTDI_{vol}$ of 63.95 mGy and a DLP of 1023.14 mGycm.

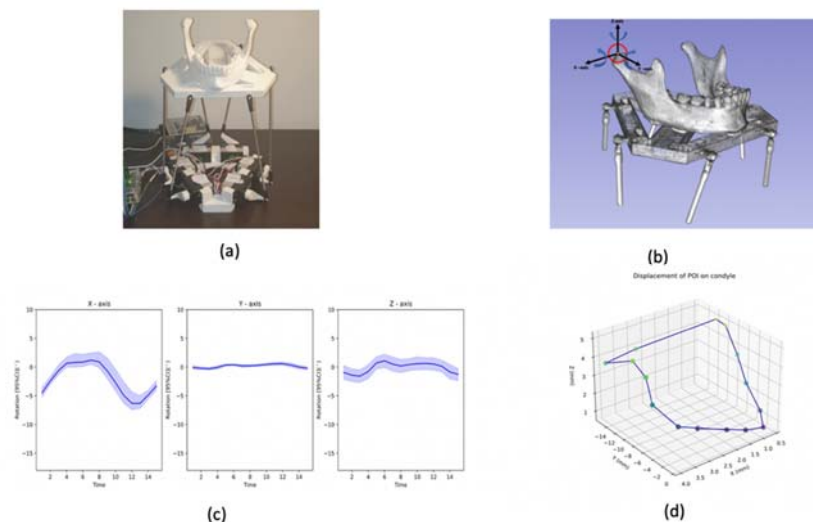


Figure 1: (a) Image of the jaw phantom (b) volume rendering of the

phantom showing a point of interest on the condyle (c) plot of cardan angles (d) 3D plot of the displacement of point of interest on the condyle.

Conclusion

A framework is proposed to use 4D CT-scanning as a usable methodology to improve the follow-up on the revalidation of patients that underwent a total temporomandibular joint replacement. A novel type of scanning phantom was also introduced, which allows six degrees-of-freedom (three translations and three rotations), with which mandibular movement can be simulated more accurately. This technique can allow us to evaluate the exact and precise working of temporomandibular joint prostheses and check their performance, whilst taking into consideration their design and placement. Organ doses are like those during a clinical head CT scan.

References

- [1] N.K.G. De Meurechy, P.J. Loos, M.Y. Mommaerts, Postoperative Physiotherapy After Open Temporomandibular Joint Surgery: A 3-Step Program, *J. Oral Maxillofac. Surg.* 77 (2019) 932–950. <https://doi.org/10.1016/j.joms.2018.12.027>.
- [2] P.A. Yushkevich, J. Piven, H.C. Hazlett, R.G. Smith, S. Ho, J.C. Gee, G. Gerig, User-guided 3D active contour segmentation of anatomical structures: Significantly improved efficiency and reliability, *Neuroimage*. 31 (2006) 1116–1128. <https://doi.org/10.1016/J.NEUROIMAGE.2006.01.015>.
- [3] C. Lee, K.P. Kim, W.E. Bolch, B.E. Moroz, L. Folio, NCICT: a computational solution to estimate organ doses for pediatric and adult patients undergoing CT scans, *J. Radiol. Prot.* 35 (2015) 891. <https://doi.org/10.1088/0952-4746/35/4/891>.

Simulation platform for contrast-enhanced dual-energy mammography

Katrien Houbrechts¹, Liesbeth Vancoillie², Lesley Cockmartin², Nicholas Marshall^{1,2}, Hilde Bosmans^{1,2}

¹ KU Leuven, Department of Imaging and Pathology, Division of Medical Physics & Quality Assessment, Herestraat 49, 3000 Leuven, Belgium

² UZ Leuven, Department of Radiology, Herestraat 49, 3000 Leuven, Belgium

ABSTRACT - Additional research is necessary for contrast-enhanced dual-energy mammography (CEDM) to investigate its potential use in the screening of specific subgroups of women, such as in women with dense breasts. Virtual clinical trials are theretofore a promising tool. Since there is currently no validated publicly available complete pipeline that can simulate this modality, we have extended an existing framework named VICTRE. The implementation of CEDM was validated with the simulation of a CIRS 022 phantom and anthropomorphic breast phantoms with cancerous lesions.

KEY WORDS – Breast imaging, virtual clinical trials, contrast-enhanced dual-energy mammography

1. Introduction

The diagnostic performance of the current breast screening technique depends heavily on the breast density. Contrast-enhanced dual-energy mammography (CEDM) is an emerging modality that has been proven to have a superior ability to depict cancers in dense breast tissue. Iodinated contrast medium is injected to map the abnormal blood flow related to neovascularity associated with breast cancer. A pair of low and high-energy images is obtained after which they are combined to enhance contrast uptake areas [1]. Before new imaging modalities such as CEDM can be applied in practice, extensive testing is needed to investigate their diagnostic benefits and potential side effects compared to the standard care. An upcoming alternative for time-consuming, expensive clinical trials are virtual clinical trials (VCTs) which use a computerized simulation framework to model the complete imaging chain [2]. This study will adapt an open-source simulation framework named VICTRE which is designed to simulate full-field digital mammography (FFDM) and digital breast tomosynthesis (DBT) [3], to simulate contrast-enhanced images. This would then allow to investigate the role of CEDM in personalized screening where women will be classified in specific subgroups based on their individual risk of breast cancer to provide different screening recommendations.

2. Materials and methods

a. CEDM simulations

A voxel model of the CIRS 022 phantom was created and virtually imaged with a low- and high-energy spectrum under the same conditions as the images taken on a Siemens MAMMOMAT Revelation system with the TiCEM application. To expand the VICTRE pipeline with the Siemens CEDM application, a high-energy spectrum file was generated with SpekPy [4]. Regarding the breast composition, material files of specific concentrations of iodine taken up by glandular tissue were generated using PENELOPE 2006. Subsequently, a Fortran script was used to turn these PENELOPE 2006 material files into MC-GPU material files. A MATLAB script was created to adjust the original mass models to simulate non-homogeneous iodine uptake which gives the ability to study the impact of the enhancement morphology characteristics of lesions. To be able to match the number of histories in the simulation with the number of x-rays in the real acquisition, a conversion factor of number of histories per mAs for each spectrum was obtained from the ratio of the experimentally measured air kerma value and the simulated air kerma value, namely the dose tallied in a 3x3x3mm³ air volume at 1m from the source. The ultimate goal is to make the VICTRE pipeline able to replicate the main characteristics of experimentally acquired CEDM images.

b. Subtraction algorithm

To allow the simulation of each step of the CEDM technique with the VICTRE pipeline, a subtraction algorithm was implemented in Python to obtain a recombined image (*DE*) by performing a weighted subtraction of the logarithmic transform of the low-energy (*LE*) and high-energy (*HE*) image as indicated in the formula:

$$DE = \log HE - \omega \cdot \log LE$$

The optimal weighting factor ω is dependent on two parameters: breast thickness and spectrum (kV and anode/filter combination). Since these parameters are different for each patient, a method to define this patient specific weighting factor, described by Huang *et al.* [5], was implemented. This will also consider the fact that the

weighting factors near the periphery of the breast, where the breast is thinner, should be different from those in the center. This thickness variation could be mapped by determining the length of the x-ray, defined by a straight line that connects each detector pixel with the x-ray source, which intersects the breast volume as illustrated in Figure 1.A. To include the spectrum dependence, homogeneous phantoms composed of glandular and adipose tissue were generated where both the thickness (2 to 8cm at 1cm interval) and the glandularity (0% to 100% at 20% intervals) were varied. These phantoms were imaged with a LE spectrum (29kVp, W target, 50 μ m Rh filter, 1mm Be window) and a HE spectrum (49kVp, W target, 1mm Ti filter, 1mm Be window).

3. Results and discussion

a. Subtraction algorithm

To include the dependence of weighting factor ω on the breast thickness, an image-specific breast thickness map (Figure 1.B) was calculated. Next, the weighting factor for each thickness could be obtained by plotting the logarithm of the measured pixel values in the LE and HE image of the homogeneous phantoms at a given breast density and thickness, as shown on the left in Figure 2. Consequently, the weighting factor ω for each breast thickness was determined as the slope of the linear fit, summarized in the right graph of Figure 2.

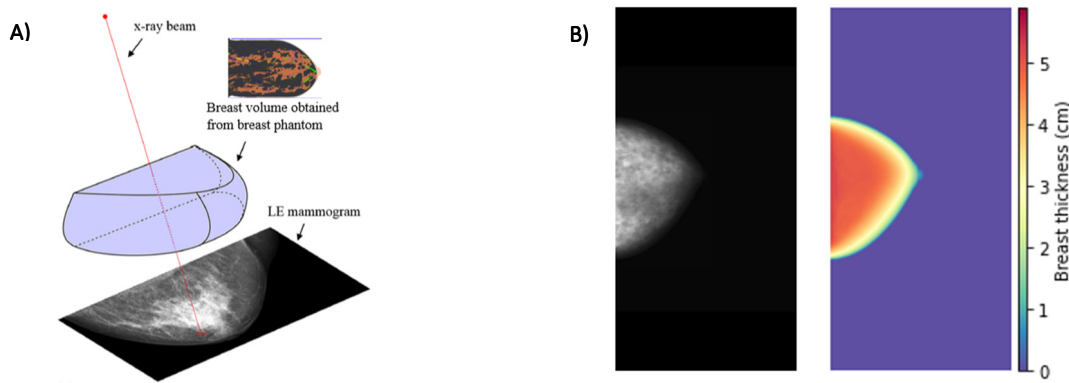


Figure 1: A) Illustration of breast thickness estimation based on the path lengths of the x-rays through the breast volume [5], B) example of a breast thickness map

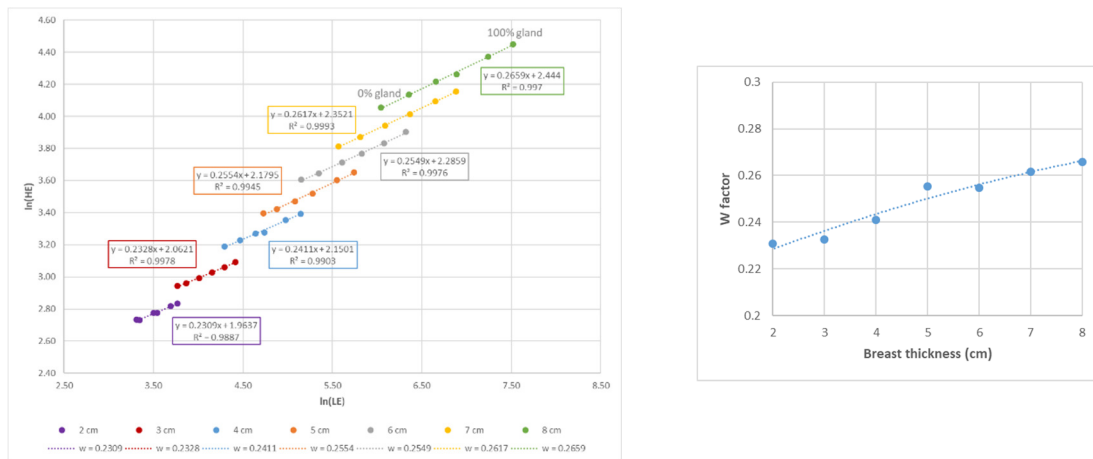


Figure 2: The plot of log signal intensity of HE spectrum against log signal intensity of LE spectrum for varying breast thicknesses (2 to 8 cm) and varying breast glandularities (0 to 100%).

b. CEDM simulations

In Figure 3, the recombined images of the virtual CIRS 022 phantom are obtained with (a) a constant weighting factor ω of 0.25 and (b) a thickness-specific ω -map. The red line illustrates the size of the phantom defined on the LE image, indicating some information loss at the boundaries when a constant weighting factor is used.

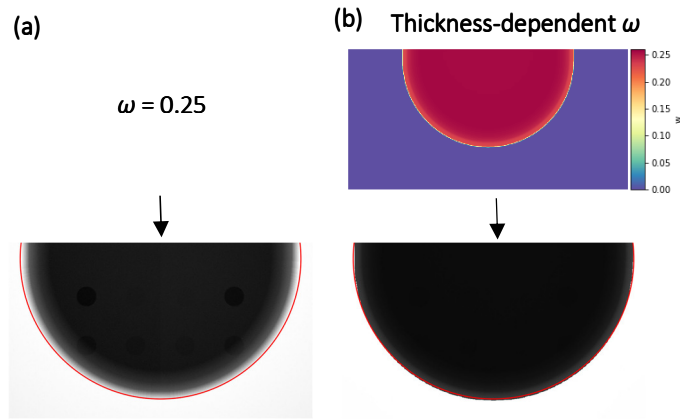


Figure 3: The impact of (a) constant and (b) thickness dependent weighting factor on the recombined image of a CIRS 022 phantom

To check if the pipeline could generate realistic CEDM images, virtual images of the CIRS 022 phantom were acquired (Figure 4, bottom row) and compared to experimentally acquired images (Figure 4, top row). The two central glandular inserts of the phantom nicely disappear in the recombined image.

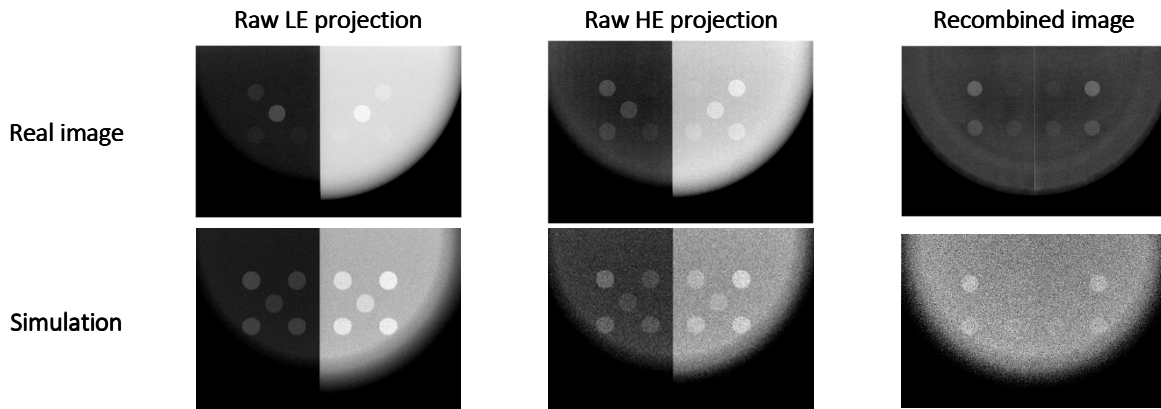


Figure 4: Real and virtual CEDM images of the CIRS 022 phantom

Last, a heterogeneous breast with five mass lesions was simulated to mimic a clinical case. The average iodine uptake of the lesions displayed in Figure 5 are chosen to be $3\text{mg}/\text{cm}^3$. The VCT is able to simulate the main goal of CEDM i.e. to cancel the contrast of tissues in regions without iodine through the combination of the two mammograms.

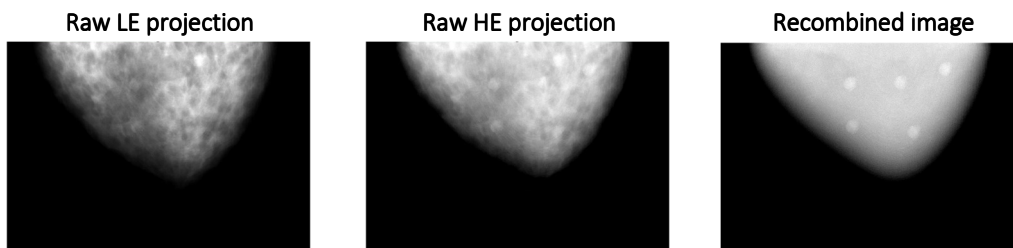


Figure 5: A heterogeneous breast with five iodinated masses imaged with CEDM

4. Conclusion

A continuous development in breast imaging techniques also requires a continuous development of the VCT frameworks. This study showed promising results in the ability to simulate realistic and clinically relevant CEDM images, which can be a big help to further optimize and validate this technique. The implementation of CEDM in the VICTRE framework will be used, after a quantitative validation, to perform a VCT to investigate the role of CEDM in personalized screening.

References

- [1] Petrillo A, Fusco R, Vallone P, Filice S, Granata V, Petrosino T, Rosaria Rubulotta M, Setola SV, Mattace Raso M, Maio F, Raiano C, Siani C, Di Bonito M, Botti G. Digital breast tomosynthesis and contrast-enhanced dual-energy digital mammography alone and in combination compared to 2D digital synthesized mammography and MR imaging in breast cancer detection and classification. *Breast J.* 2020 May;26(5):860-872. doi: 10.1111/tbj.13739. Epub 2019 Dec 30. PMID: 31886607.
- [2] Abadi E, Segars WP, Tsui BMW, Kinahan PE, Bottenus N, Frangi AF, Maidment A, Lo J, Samei E. Virtual clinical trials in medical imaging: a review. *J Med Imaging (Bellingham).* 2020 Jul;7(4):042805. doi: 10.1117/1.JMI.7.4.042805. Epub 2020 Apr 11. PMID: 32313817; PMCID: PMC7148435.
- [3] Badano A, Graff CG, Badal A, et al. Evaluation of Digital Breast Tomosynthesis as Replacement of Full-Field Digital Mammography Using an In Silico Imaging Trial. *JAMA Netw Open.* 2018;1(7):e185474. doi:10.1001/jamanetworkopen.2018.5474
- [4] Poludniowski, G., Omar, A., Bujila, R. and Andreo, P. (2021), Technical Note: SpekPy v2.0—a software toolkit for modeling x-ray tube spectra. *Med. Phys.*, 48: 3630-3637. <https://doi.org/10.1002/mp.14945>
- [5] Hailiang Huang, David A. Scaduto, Chunling Liu, Jie Yang, Chencan Zhu, Kim Rinaldi, Jason Eisenberg, Jingxuan Liu, Mathias Hoernig, Julia Wicklein, Sebastian Vogt, Thomas Mertelmeier, Paul R. Fisher, Wei Zhao, "Comparison of contrast-enhanced digital mammography and contrast-enhanced digital breast tomosynthesis for lesion assessment," *J. Med. Imag.* 6(3), 031407 (2019), doi: 10.1117/1.JMI.6.3.031407

Patient eye lens dose during neurointerventional procedures in Belgium

J. Dabin¹, H. Bosmans², L. Eloot³, H. Franssen³, E. Gielen⁴, S. Heye^{2,4}, A. Houben⁴, W. Schoonjans¹, L. Stockx⁴, L. Struelens¹

¹*Belgian Nuclear Research Centre, Belgium*

²*UZ Leuven, Belgium*

³*AZ Sint-Lucas, Belgium*

⁴*Ziekenhuis Oost-Limburg, Belgium*

ABSTRACT – Patient eye lens dose were measured during 69 procedures in three Belgian hospitals. Average (max) doses to the left and right eyes were 36 (300) and 58 (380) mSv. All measured doses were below the limit for radio-induced eye lens opacities (500 mGy) but could be close to it, even on recent X-ray systems. This is of concern for - younger - patients who undergo multiple procedures, and should be incorporated into the patient follow-up.

KEY WORDS – neurointervention; eye lens dose; patient dosimetry; tissue reaction; patient follow-up

Introduction

Neurointerventional procedures are of great benefit for the patients thanks to their low invasiveness but they bear increased risks of tissue reactions owing to their duration and complexity. Cases of tissue reactions are documented in the literature and several studies characterised the dose delivered to the patient's skin. However, reports of the dose to the eye lens of the patient are still scarce. This study aimed to investigate (i) the level of dose to the patient eye lens and (ii) the correlation between eye lens dose and procedure parameters.

Materials and methods

Patients' eye lens doses were monitored with dedicated eye lens dosimeters during 69 neurointerventional procedures in three Belgian hospitals. For each procedure, demographic and procedure characteristics were collected, including the Kerma-area product ($P_{K,A}$) and the cumulative air kerma at the reference point ($K_{a,r}$). Radiation dose structured reports (RDSRs) were collected when available. During the first study phase, a total of 40 procedures were monitored in three hospitals. During the second phase, measurements were continued in 2 hospitals after installation of a new X-ray unit. Twenty nine additional procedures were monitored. Statistical differences between groups were tested with a Wilcoxon test.

Results

During the first study phase, the dose to the eyes ranged from 0.02 to 380 mSv (Fig1). The dose to the right eye was significantly greater than the dose to the left eye (on average, 38 and 88 mSv to the left and right eye, $p < 0.01$). No significant difference in dose was observed between the hospitals. During the second phase (Fig1), the doses to the left eye ranged from 4 to 310 (mean: 38) mSv and the right eye from 4 to 58 (mean: 15) mSv. These doses were significantly lower than during the first phase ($p < 0.001$). No significant difference were observed between both eyes but doses were significantly lower in hospital 1 (16 and 15 mSv for left and right eye, respectively) compared to hospital 2 (63 and 15 mSv, respectively; $p = 0.02$).

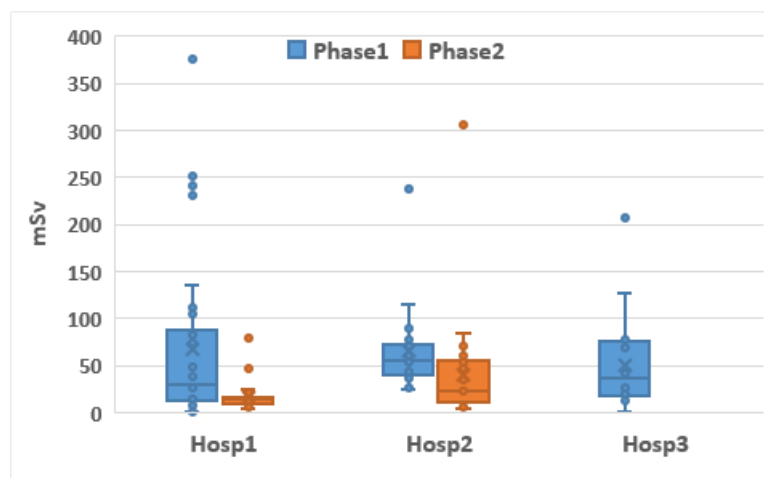


Figure 1: eye lens dose (mSv) distributions (left and right eye pooled) during neurointerventional procedures. Phase 1 and 2 indicates the installation of a new X-ray unit.

The correlations between the eye lens dose and the $P_{K,A}$ or the $K_{a,r}$ cumulated over the complete procedure were poor and could not be used to predict the eye lens dose. For those procedures with RDSRs, the availability of the $P_{K,A}$, or the $K_{a,r}$, and the beam angulation for each irradiation event lead to better prediction of the eye lens dose.

Conclusion

All measured doses were below the International Commission for Radiological Protection (ICRP) limit for radio-induced eye lens opacities (500 mGy). However, the maximum dose could be high and come close to the limit. Considering the relatively small number of procedures monitored, this suggests that the 500-mGy threshold can be exceeded during a single procedure. Therefore, the risk of exceeding it should not be overlooked, in particular for - younger - patients who undergo multiple procedures, sometimes over a short period. This should be accounted for in the patient follow-up.